



Conformational activation of ribosome recycling by intra- and inter-molecular dynamics of RRF

Guangtao Song^{a,1}, Benjin Xu^{a,b,c,1}, Huigang Shi^{b,d,1}, Yong Zhang^a, Dejiu Zhang^a, Xintao Cao^{a,b}, Zengrui Liu^{a,e}, Ran Guo^{a,e}, Yan-Zhong Guan^e, Yanhui Chu^f, Xinzheng Zhang^{b,d,*}, Jizhong Lou^{a,b,**}, Yan Qin^{a,b,**}

^a Key Laboratory of RNA Biology, CAS Center for Excellence in Biomacromolecules, Institute of Biophysics, Chinese Academy of Sciences, 15 Datun Road, Chaoyang District, Beijing 100101, China

^b University of Chinese Academy of Sciences, Beijing 100049, China

^c Laboratory Medicine Department in Fenyang College of Shanxi Medical University, Fenyang 032200, China

^d National Laboratory of Biomacromolecules, CAS Center for Excellence in Biomacromolecules, Institute of Biophysics, Chinese Academy of Sciences, Beijing 100101, China

^e Department of Physiology, Mudanjiang Medical University, Mudanjiang 157011, China

^f Heilongjiang Key Laboratory of Anti-Fibrosis Biotherapy, Mudanjiang Medical University, Mudanjiang 157011, China

ARTICLE INFO

Article history:

Received 27 March 2020

Received in revised form 21 May 2020

Accepted 27 May 2020

Available online 30 May 2020

Keywords:

Ribosome recycling factor

Molecular flexibility

Domain orientation

Molecular dynamics simulation

Single-molecule FRET

Cryo-EM

ABSTRACT

Ribosome recycling is the final step of the cyclic process of translation, where the post-termination complex (PoTC) is disassembled by the concerted action of ribosome recycling factor (RRF) and elongation factor G (EF-G) in the sub-second time range. Since, however, both the RRF and PoTC display highly dynamic action during this process, it is difficult to assess the molecular details of the interactions between the factors and the ribosome that are essential for rapid subunit separation. Here we characterized the molecular dynamics of RRF and PoTC by combined use of molecular dynamics simulations, single molecule fluorescence detection and single-particle cryo-EM analysis, with time resolutions in the sub-millisecond to minute range. We found that RRF displays two-layer dynamics: intra- and inter-molecular dynamics during ribosome splitting. The intra-molecular dynamics exhibits two different configurations of RRF: 'bent' and 'extended'. A single-site mutant of RRF increases its propensity to the 'extended' conformation and leads to a higher binding affinity of RRF to the PoTC. The inter-molecular dynamics between RRF and EF-G in the PoTC reveals that the domain IV of EF-G pushes against the domain II of RRF, triggering the disruption of the major inter-subunit bridge B2a, and catalyzes the splitting.

© 2020 Published by Elsevier B.V. All rights reserved.

1. Introduction

The protein translation is a four-step cyclic process in which the genetic information encoded in an mRNA is converted into a sequence of amino acids in a protein catalyzed by the ribosome [1–5]. When a ribosome reaches a termination codon on an mRNA, the newly synthesized polypeptide is released from the ribosome, forming a post-termination complex (PoTC). The bacteria use ribosome recycling factor (RRF) together with elongation factor G (EF-G) and GTP to disassemble the PoTC, freeing the ribosome for the next round of translation (Figs. 1A and S1) [2,6,7]. Since RRF ablation induces severe decrease of protein

biosynthesis *in vivo* [8], the factor and recycling step have been regarded essential for bacterial life.

RRF is a basic protein composed of about 185 amino acids. Structures of RRF from several species reveal that it is normally composed of two domains which adopt an L-shape. Domain I, the long arm of the "L", consists of residues 1–28 and 107–185, forming three long α -helix bundles. Domain II, the short arm, consists of residues 32–102, forming a β - α - β -sheet motif (Figs. 1B and S2A) [9,10]. The two domains are connected by two highly flexible linkers and relative orientation of domain II differs substantially in various structures (Figs. 1B and S2B). An early hydroxyl radical probing study suggests that RRF binds to the ribosome complex at a well-defined location in the subunit interface cavity [11]. Cryo-electron microscopy (cryo-EM) studies of *T. thermophilus* RRF (ttRRF) bound *E. coli* ribosomes showed that RRF was in two very different positions (Fig. S2C) [12]. Studies on the kinetic mechanism for ribosome recycling revealed that ribosome splitting required EF-G binding to an already RRF-containing ribosome, resulting in a maximal recycling rate of 25 s⁻¹ at the cost of about one GTP hydrolyzed per splitting event [13]. Therefore, the RRF intra- and inter-molecular dynamics may affect the functions of the ribosome and the factors during recycling. However,

* Correspondence to: X. Zhang, National Laboratory of Biomacromolecules, CAS Center for Excellence in Biomacromolecules, Institute of Biophysics, Chinese Academy of Sciences, Beijing 100101, China.

** Correspondence to: J. Lou, Y. Qin, Key Laboratory of RNA Biology, CAS Center for Excellence in Biomacromolecules, Institute of Biophysics, Chinese Academy of Sciences, 15 Datun Road, Chaoyang District, Beijing 100101, China.

E-mail addresses: xzzhang@ibp.ac.cn (X. Zhang), jlou@ibp.ac.cn (J. Lou),

qiny@ibp.ac.cn (Y. Qin).

¹These authors contributed equally to this work.

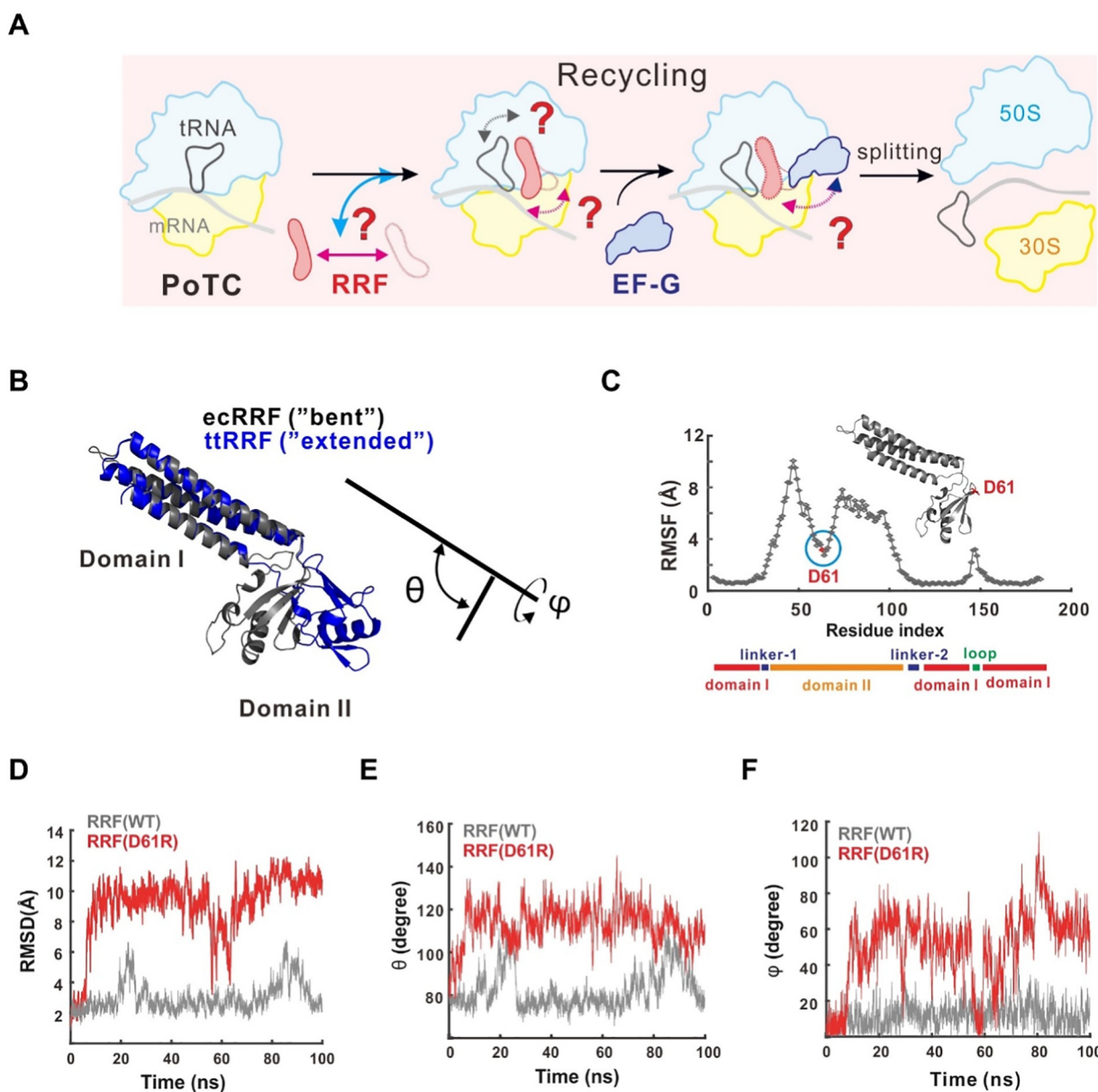


Fig. 1. Intra-molecular dynamics of RRF: 'bent' and 'extended' conformations. (A) Schematic model of ribosome recycling and the question marks remained. (B) Observed structures of *E. coli* RRF (ecRRF) (PDB: 4V9D) and *T. thermophilus* RRF (ttRRF) (PDB: 3j0d). Domain I of these structures is superimposed. (C)–(F) Structural flexibility of ecRRF and its D61R mutant in MD simulation. RMSF (C) and RMSD (D) of the RRFs, and changes of bending angle θ (E) and rotation ϕ angle (F) during simulation are indicated. The angle ϕ of the ecRRF in PoTC-RRF (PDB: 4V9D) is defined as 0.

the complicated and fast kinetics of recycling step makes it difficult to study the molecular details about the interactions between these protein factors and the ribosome. In the present study, by combined use of molecular dynamics (MD) simulations, single-molecule fluorescence energy transfer (smFRET), single-particle cryo-EM reconstruction, and biochemical methods, we characterized the detailed molecular dynamics of RRF and PoTC complexes on sub-millisecond-to-minute time scales (Fig. S1). Based on these data, we tried to reconstruct a kinetic model for the conformational activation of ribosome recycling.

2. Materials and methods

2.1. Construction, purification and labeling of RRF proteins

RRF from *E. coli* was cloned into vector pET-22b(+) as previously described [14]. Its single-site mutants were constructed with a MutanBEST

Kit and Site-Directed Mutagenesis kit (TaKaRa). All RRF proteins were expressed in *E. coli* BL21(DE3) induced with 0.5 mM IPTG, at 37 °C for 4 h. A nickel column was used in the first step of purification. The concentrated samples were further purified with a Sephadex G-200 column (GE Healthcare) in a buffer containing 20 mM Tris-HCl, pH 7.6, 500 mM NaCl and 4 mM 2-mercaptoethanol. RRF(S73C) was labeled with Cy3- and Cy5-maleimide (GE Healthcare) following the manufacturer's recommendations. Briefly, an equimolar mixture of Cy3- and Cy5-maleimide (GE Healthcare) dissolved in dimethyl sulfoxide (DMSO) was added to the reaction mixture such that the Cy3- and Cy5-maleimide were both in a 10-fold molar excess over RRF. The reaction was incubated for 4 h in the dark at room temperature. The unreacted Cy3- and Cy5-maleimide was then removed by using Zeba™ Spin Desalting Columns (Thermo Scientific). Alexa 488 labeled RRF proteins were obtained by reaction of the unique cysteine residue (C16) with the maleimide derivative of Alexa 488.

2.2. Single-molecule fluorescence experiments

Single-molecule fluorescence experiments were performed with an objective-type total internal reflection fluorescence microscope. For the smFRET study on RRF dynamics experiments, Cy3/Cy5-labeled and N-terminal biotin-tagged RRFs were directly immobilized on the polyethylene glycol-passivated cover-glass surface through streptavidin–biotin interaction. For the single-molecule study of the RRF binding, purified PoTC were first immobilized *via* hybridization between its mRNA with the pre-immobilized biotinylated DNA oligonucleotides. 10 nM Alexa-488 labeled RRF was incubated in the chamber, allowing the RRF molecules to bind the surface immobilized PoTC. After 5 min of incubation, unbound RRF were washed away with the imaging buffer. Imaging was performed at room temperature in a buffer (20 mM HEPES, pH 7.8, 8.2 mM MgSO₄, 80 mM NH₄Cl, 100 mM KCl, 2 mM MgCl₂). An oxygen scavenging system (2 units μl⁻¹ glucose oxidase, 20 units μl⁻¹ catalase, 0.8% β-D-glucose and 2 mM Trolox (Sigma-Aldrich)) was used in all experiments to prevent the organic fluorophores from severe photo-fatigue. The time resolution for all the experiments was 100 ms. Detailed methods of smFRET data acquisition and analysis were described in previous studies [15]. The FRET efficiency of a single molecule was approximated as $FRET = I_A / (I_D + I_A)$, where I_D and I_A are the background and leakage-corrected emission intensities of the donor and acceptor, respectively. The histograms of the FRET of the RRF were obtained by averaging the first 50 frames of each FRET trace for every individual molecule after manually filtering photo-bleaching effects. For RRF binding experiments, each single-molecule trajectory was fit to a hidden Markov model with an initial guess of 2 states (Bound and release states, respectively). Time resolved population histograms of the bound state (bin size of 0.1 s) were further fitted with single exponential decay to obtain the bound lifetime of the RRF molecules.

2.3. Molecular dynamics (MD) simulations

The initial conformations of the RRF were taken from the solved structures (PDB code 3J0D (for ecRRF) and 4V9D (for tRRF)). The model of D61R mutated ecRRF is obtained by *in-silico* mutation from WT ecRRF structure using the MUTATE plugin of VMD software [16]. These initial structures were solvated in rectangular TIP3P water boxes respectively (~10.6 × 7.5 × 5.7 nm³ for ecRRF and ~11.0 × 8.1 × 5.8 nm³ for tRRF). Two angles θ and φ were used to describe the relative position of domain I and II of RRF. The axis of each domain is defined by connecting the hinge (center of mass (COM) of residue 30, 31, 104, 105) to a point at the other end of the domain (COM of residues 5, 139, and 156 for domain I and residues 51, 56, 68, 78, and 98 for domain II), these definitions are the same as these used in previous MD simulations [4]. The bend angle θ is simply the dot product of unit vectors along the two domain axes. The rotation angle φ is calculated as an angle between the axis of domain II and the plane defined by the two axes in the cryo-EM structure of ecRRF after aligning the domain I in MD trajectories to that of cryo-EM structure of ecRRF. Here we define $\varphi = 0^\circ$ for the initial structure of ecRRF from PDB: 4V9D. The model of the PoTC·RRF-EF-G complex is constructed by superimposing the known structure of PoTC·RRF (PDB:4V9D) and EF-G (PDB:4V9P) to the electron microscopy map of PoTC·RRF-EF-G ternary complex (EMD: 8413). There are some clashes between domain II of RRF and domain IV of EF-G. Taking into account the interdomain flexibility of EF-G and RRF, we captured one snapshot structure of RRF from MD simulation and made small adjustment of the domain IV of EF-G to remove these clashes. A truncated model of ribosome complex including tRNA, RRF, EF-G, tRNA, mRNA, 23S rRNA (185–255, 370–426, 800–1148, 1356–1375, 1645–1708, 1750–2788), L1, L11, L14, L16, L27, L28, L33, L36, 16S rRNA (29–60, 152–170, 313–555, 980–1060, 1195–1230, 1398–1437, 1462–1506), S12, S14, S19, were used in MD simulation after balancing the model validity and computational cost. It is solvated in a 21.8 × 24.9 × 22.0 nm³ TIP3P water box, forming a system ~1.16 million atoms. All these solvated systems are neutralized using Na⁺ and Cl⁻

ions (~0.15 M). Amber ff14SB force field is used for the protein and nucleic acids, including bsc0 and OL3 modification for RNA and OL1 and OL4 modification for RNA [17]. Under periodic boundary condition, a 12 Å cut-off (switching 10–12 Å) was used for van der Waals interactions, and Particle Mesh Ewald summation was used to calculate the electrostatic interactions. The NAMD package was used for energy minimizations and molecular dynamics simulations. After multi-step energy minimization to avoid possible clashes, the system was then equilibrated in 3 steps: 2 ns simulation with strong constrain of heavy atoms of protein/nucleic, 2 ns simulation with strong constrain of protein/RNA backbone atoms and 4 ns simulation with weak constrain of protein/nucleic backbone atoms. Subsequently, ~100 ns free molecular dynamics simulations on NPT ensemble were performed to investigate the dynamics structure of RRF. During the simulations, the temperature was controlled at 300 K by Langevin method and pressure was controlled at 1 atm by Langevin piston method. SHAKE method was used on all hydrogen-containing bonds to allow a 2 fs time step. The simulation trajectories were analyzed with VMD program [18].

2.4. Cryo-EM data collection and structure determination

The PoTC·RRF complex was prepared as described before [14]. The sample was diluted to 150 nM with 10 μM RRF in buffer (20 mM HEPES pH 7.6, 8.2 mM MgSO₄, 80 mM NH₄Cl, 4 mM 2-mercaptoethanol). Five pmol of ribosomes were loaded onto a 10% SDS-PAGE gel to observe the binding of RRF and its mutant to the PoTC complex. Approximately 3 μl aliquots sample were applied to glow-discharged GIG M322 grids (300 mesh, R2/2) with a thin layer of carbon film coated. The grids were plunged into liquid ethane after 3s' blotting with blotting force of -2 by an automatic plunge device (FEI Vitrobot IV). Data was collected in a 200 keV TEM (Talos F20) equipped with direct detector DE-20 at a magnification of 28,000×, yielding a pixel size of 1.58 Å. The dose rate was 28 e⁻/Å² s and the exposure time was 1 s with a total of 16 frames in each image. The beam-induced motion was corrected by MOTIONCORR [19]. The defocus and astigmatism parameters were estimated by CTFIND3. For PoTC + RRF(D61R), 119,135 particles were boxed by EMAN2 [20] from 878 micrographs and were subjected to reference free 2D classification [21]. 110,549 particles in good classes were kept for 3D classification using a low-pass filtered EM map of 70S ribosome initiation-like complex with fMet-tRNA^{fMet} at the P site as an initial model [22]. The 3D classification produced 4 good reconstructions in 5 classes. Among these four reconstructions, three reconstructions have a similar hybrid ribosome conformation with P/E tRNA and the other reconstruction has a classical ribosome conformation with P/P tRNA. 88,648 particles from three classes of hybrid ribosome yielded a 9.0 Å map based on the gold standard Fourier shell correlation (FSC) with 0.143 threshold. 21,901 particles of classical ribosome yielded a 10.3 Å map. For 70S + RRF(D61R), 236,125 particles were boxed from 700 micrographs and subjected to reference free 2D classification. 217,991 particles in good classes were subject to 3D classification against scaled and low-pass filtered PoTC·RRF (D61R). The 3D classification produced 3 good reconstruction in 4 classes and yielded a 6.0 Å map with well-defined RRF(D61R) density. For PoTC, 282,290 particles were boxed from 708 micrographs and were subjected to reference free 2D classification. 187,868 particles in good classes were kept for 3D classification. 61,721 particles were selected after 3D classification which yielded a 6.3 Å hybrid ribosome and 29,994 particles were selected which yielded 7.1 Å classical ribosome. For PoTC + RRF(WT), 142,239 particles were boxed from 294 micrographs for reference free 2D classification. 97,968 particles were kept and were subjected to 3D classification. The 5 good reconstructions in 5 classes yielded 5.0 Å hybrid ribosome without density of RRF(WT). Segmentation of the cryo-EM density was done by EMAN script. Fitting of X-ray crystal structure PoTC·RRF (4V9D) was done by Pymol and UCSF Chimera [23]. The crystal structure of ecRRF (1EK8) were fitted manually to 6 Å 70S·RRF EM density map in Chimera.

2.5. Polysome breakdown assay

Polysome was prepared from *E. coli* MRE600 as previously described [18]. Polysome (0.2–0.6 A_{260} units) was incubated with puromycin, RRF, EF-G and GTP in 200 μ l of RRF buffer (20 mM Hepes-KOH (pH 7.6), 8.2 mM $MgSO_4$, 80 mM NH_4Cl , 4 mM 2-mercaptoethanol) at 30 °C for 15 min. The sedimentation profiles of reactions were obtained using sucrose density gradient centrifugation (15–45%, w/v) sucrose in RRF buffer, Beckman SW40 rotor, 36,000 rpm, 3.5 h, 4 °C. The results were analyzed by A_{254} measurement.

2.6. Directed hydroxyl radical probing assay

The Fe(II)-RRF was prepared as described before [11]. Briefly, about 50-time amount of Fe(II)-BABE was incubated with the cysteine-containing RRF mutants at 37 °C for 30 min, and the excess reagent was then removed by ultrafiltration. This Fe(II)-RRF (10 μ M) was then incubated with the PoTC (1 μ M) in RRF binding buffer at 37 °C for 10 min, then on ice for 5 min. 1 μ l of 250 mM ascorbic acid and 1 μ l of 2.5% hydrogen peroxide were then added to 50 μ l of the Fe(II)-PoTC·RRF and incubated on ice for 10 min. The reaction was stopped by adding 2.5 μ l of 80 mM thiourea. The rRNA was precipitated with 0.3 M NaOAc and extracted with trizol reagent (Invitrogen). The location of 16S and 23S rRNA backbone cleavage was detected by primer extension with reverse transcriptase. Extension products were resolved by 8% urea-PAGE (8 M urea) and analyzed with a Molecular Dynamics Storm PhosphorImager (GE Healthcare).

3. Results and discussion

3.1. Intra-molecular dynamics of RRF

To analyze the flexibility of RRF, we first performed MD simulations of *E. coli* RRF (ecRRF) (Fig. 1C–F) and *T. thermophilus* (ttRRF) (Fig. S3) extracted from PoTC complexes. The average root-mean-square fluctuation (RMSF) (Fig. 1C) and root-mean-square deviation (RMSD) (Fig. 1D) for the backbone atoms were used to describe the overall dynamics and local mobility of the molecule, respectively. The relative orientation of the two domains of RRF was determined by two angles (θ and φ), as described previously [24]. The angle θ is the bending angle between domain I and II, while the angle φ is the rotation of domain II around domain I (Fig. 1B). For the *E. coli* RRF (ecRRF), the overall conformation was relatively stable (Fig. 1D, gray curve). The angle θ fluctuated between 80° and 100°, while the angle φ fluctuated around 10° (Fig. 1E and F, gray curve). Similar results could be obtained when repeated simulation was conducted (Fig. S3). For ttRRF, a conformational change occurred rapidly within 20 ns of simulations, where the angle θ decreased from 140° to 100°, and the angle φ decreased from 60° to nearly 10° (Fig. S4A–C). That is, the ecRRF conformation was initially in the ‘bent’ form and changed little during the simulation. In contrast, the ttRRF conformation was initially in the ‘extended’ form and changed to the ‘bent’ form so that the final equilibrated conformation was much closer to that of the ‘bent’ ecRRF form (Fig. S4D).

Since the ‘bent’ and ‘extended’ conformation differ from each other by the relative orientation of domains I and II, the linkers of the two domains and regions in the vicinity of the linkers may play important functional roles. Especially, the RMSF fluctuation of residues around Asp61 of domain II, which are close to the linkers, are much lower than the remaining parts of ecRRF (Fig. 1C), indicating that the corresponding region might be responsible for the conformation equilibrium. Previous structural studies showed that the R31A mutation in linker-1 region can induce a smaller rotation angle of domain II in RRF from *M. tuberculosis*, indicating the importance of the linker region on the dynamics of RRF [25]. We thus speculated that the charge-based interaction between Asp61 and Arg31 may tune the rotation state of domain II. To test this hypothesis, we performed MD simulations with D61R mutant of

ecRRF (Figs. 1C–F, S5–S6). As expected, the conformation of the mutant differs dramatically from that of wild type (WT) ecRRF. The RMSD of the molecule increased from 2.3 Å to around 10 Å. The bending angle between domain I and II increased from 80° to 120°, while the rotation angle changed from 10° to 60°, resulting in the ‘extended’ conformation.

To further prove these results, we developed an intra-molecular FRET signal for RRF to detect the changes in the distance between domains I and II (Fig. 2). An RRF mutant carrying two cysteines, one in its domain I (C16) and one in its domain II (S73C), was equipped with Cy3 FRET donor and Cy5 FRET acceptor fluorophores respectively, and its subsequent purification generated a dual Cy3-Cy5 labeled RRF (Figs. 2A and S7A). The conformational dynamics of RRF was then monitored by measuring the FRET signal changes between Cy3 and Cy5. We found that RRF alone sampled a stable FRET state centered at 0.78, demonstrating that free RRF was not highly dynamic and the distance between domain I and II was small (Figs. 2B and S7B). In contrast, the D61R mutation led to a broad peak at FRET 0.5, suggesting a more flexible state of the factor with large domain I-II distance (Figs. 2C–D and S7C). All these results clearly demonstrate that the charge-interaction between the linker-1 and domain II near residue 61 controls the conformation of domain II. Loss of this charge-interaction upon D61R mutation resulted in the extended RRF.

3.2. Inter-molecular dynamics of RRF

Previous smFRET measurements showed that RRF could alter the intrinsic dynamics of the ribosome, stabilizing the fully rotated, P/E hybrid configuration of the PoTC [26,27]. Structural and biochemical studies indicated that the orientation of domain II of RRF in the PoTC was essential for the subsequent EF-G binding and ribosome splitting [12]. However, the direct measurement of the binding frequency of RRF to PoTC at the single-molecule level is still limited (Fig. 3A). Here we conjugated fluorescent labels (Alexa-488) to the unique cysteine residue (C16) of RRF, and directly investigated the binding of single RRF molecules to the molecules of the surface-immobilized PoTC (Fig. 3B). Consistent with previous biochemical results, we only observed transient binding of RRF to the PoTC (Fig. 3C). To explore the kinetic basis for the PoTC·RRF interaction, we determined the binding lifetime (dwell time) by fitting the individual trajectories with the Hidden-Markov Model (Fig. 3D). Dwell-time analysis of these binding events revealed that RRF(WT) could stay around 1.5 s on PoTC (1.44 ± 0.04 s), which indicated that the kinetics of recycling was a medium-speed step in the translation cycle. Single-site mutant RRF(D61R) stayed 1.6 times longer than RRF (WT) (2.26 ± 0.07 s), indicating that RRF(D61R) bound to PoTC with higher affinity than that of RRF(WT).

To obtain more structural information on the interactions between WT or mutant RRF and PoTC, we next performed cryo-EM structural analysis of these complexes (Figs. 4A and S8). For PoTC alone, 3D classification yielded two classes of cryo-EM structures, further 3D refinement produced a 6.3 Å rotated ribosome with a hybrid P/E-site tRNA and a 7.1 Å resolution nonrotated ribosome with a classical P/P-site tRNA (Fig. S8A). The percentage of rotated ribosomes was around 67%, which was consistent with the smFRET results, indicating that PoTC underwent spontaneous intersubunit rotational movement under our conditions. For PoTC·RRF(WT) complex, the percentage of rotated ribosome was close to 100% (Fig. S8B). However, we were not able to observe good density of RRF in these structures, even though the binding of RRF was clearly indicated in the gel mobility assay (Fig. S9). In contrast, for the D61R mutant, the density of RRF inside the PoTC in the rotated state was clearly observed (Fig. S8C). This indicates that the single-site mutation (D61R) of RRF may facilitate the stable binding of RRF into the PoTC. And this point was further confirmed when we analyzed 70 S ribosome in complex with this mutant. A 6.0 Å resolution map was produced, where RRF(D61R) was in a much clearer conformation (Figs. 4A, S8D). When comparing these structures of PoTC·RRF (D61R) and 70 S·RRF(D61R), it was apparent that domain II pointed

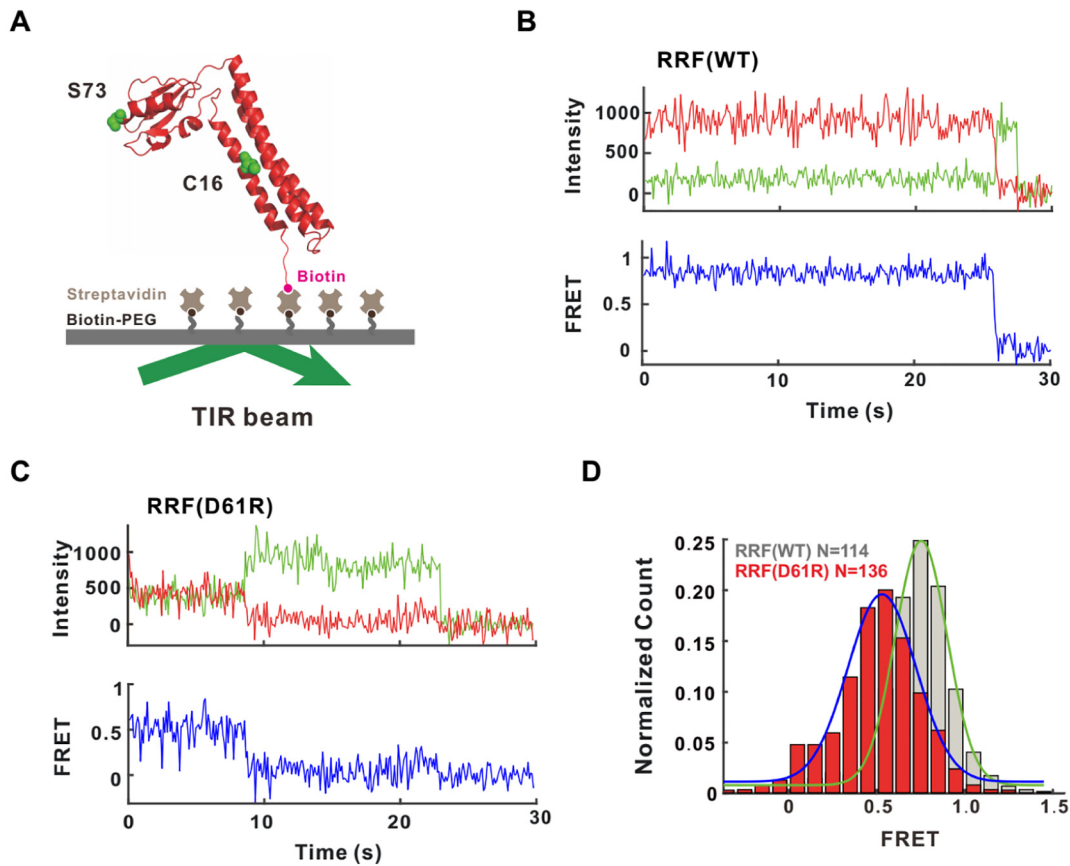


Fig. 2. smFRET study on the intra-molecular dynamics of RRF. (A) Experimental setup of the assay. (B)–(C) Typical smFRET signal traces for the ecRRF (B) and its D61R mutant (C). (D) FRET histogram of the labeled ecRRFs.

toward 50S subunit in both complexes. To certify this observation, we used directed hydroxyl radical probing of rRNA from Fe(II)-BABE modified RRF proteins bound to the PoTC [11]. RRF residues 56 and 77 were used to probe the orientation of domain II. We found that the 23S rRNA

sarcin loop (helix 95) could be cleaved from both positions of RRF(WT), and much stronger cleavage was observed from D61R mutant (Fig. 4B). These results are in agreement with the cryo-EM data that the domain II of RRF(D61R) preferred to bind to the 50S subunit, similar to that of

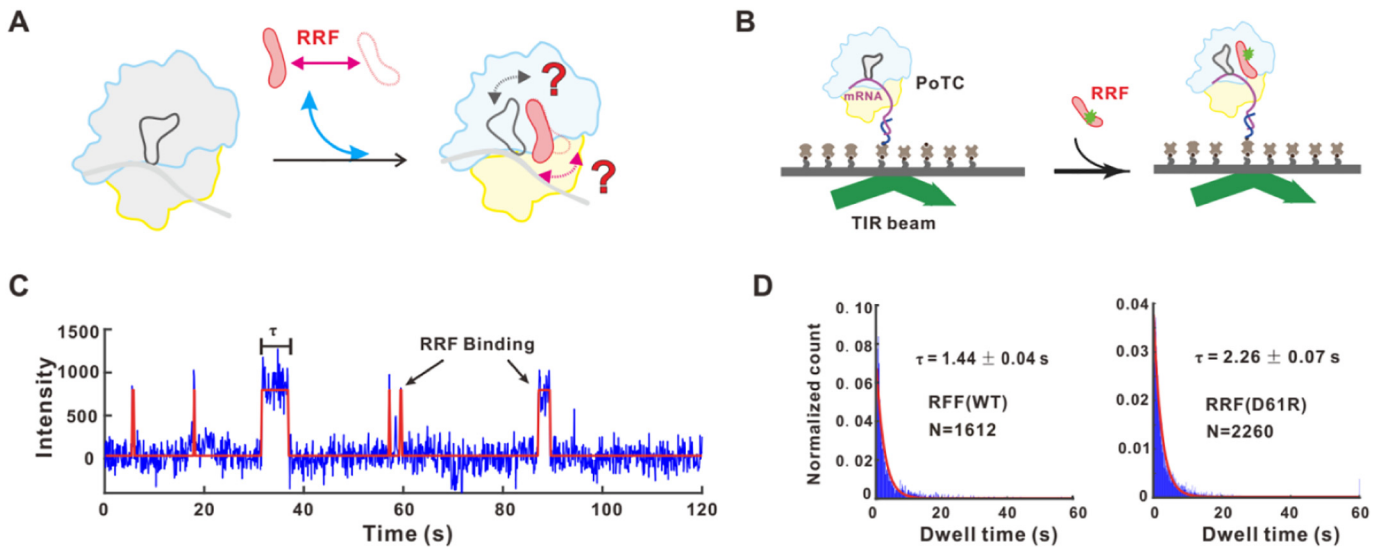


Fig. 3. Direct observation of RRF binding to PoTC. (A) Schematic model of RRF binding to PoTC and the question marks remained. (B) Experimental setup of the assay. (C) A typical single-molecule fluorescence trace, imaged at 100 millisecond time resolution at room temperature. Idealization of the fluorescence change is overlaid in red. (D) Dwell-time analysis of wild-type (WT) or D61R mutant RRF binding to PoTC.

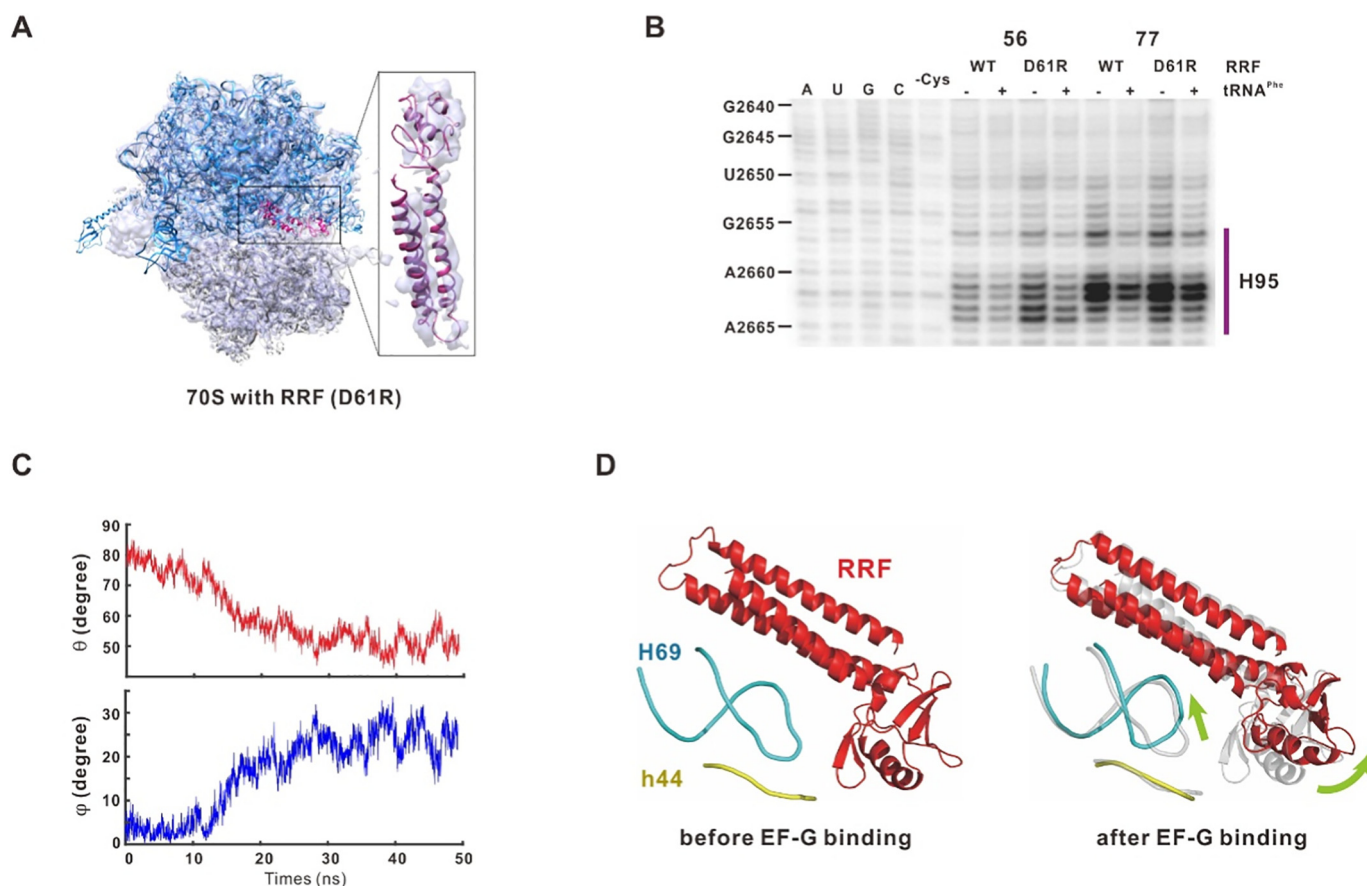


Fig. 4. Inter-molecular dynamics of RRF: conformational activation of ribosome recycling. (A) Cryo-EM map of 70S ribosome with RRF(D61R). A zoom-in view of RRF in was showed. (B) Directed hydroxyl radical probing of 23S rRNA from PoTC-RRF-Fe(II) complexes. Nucleotide numbers on the left correspond to the position of 23S rRNA. Purple vertical line on the right indicates the nucleotides bound with WT or D61R mutant RRF derivatized by Fe(II)-BABE at positions 56 and 77. (C) Conformational changes of RRF after EF-G binding in the MD simulations as observed by the shift of angles θ and ϕ . (D) Conformational changes of B2a bridge and RRF after EF-G binding in PoTC.

domain II of ttRRF inside the *E. coli* ribosome [12]. These results suggest that D61R mutation altered the dynamics of domain II and enhanced its binding to the ribosome complex. When we tested the activities of D61R mutant in ribosome recycling by measuring the reduction of naturally produced poly-PoTC [14], we found that the recycling activity was considerably compromised (Fig. S10). These results indicate that the binding of RRF(D61R) to the PoTC, although stronger than that of RRF(WT), prohibits the subsequent EF-G binding and ribosomal splitting. These results provide an explanation for the inhibitory effect of heterologous RRF on the recycling reaction [28,29].

3.3. Domain IV of EF-G pushes against domain II of RRF to catalyze ribosome splitting

To elucidate the molecular interactions between RRF and EF-G during ribosome splitting, we then performed MD simulations by generating a model system with the structures of RRF (PDB:4V9D) and EF-G (PDB:4V9P) into the PoTC structure (EMD: 8413) [30]. The resulting complex contained some small clashes between RRF domain II and EF-G domain IV. Considering the interdomain flexibility of the two factors, we adjusted the positions of EF-G domain IV to remove these clashes (Fig. S11A). After MD simulations, we found that the overall flexibility of the RRF in the PoTC was much lower than that of free RRF, mainly for the domain II (Fig. S11B). It was clear that domain II of RRF made several contacts with domain IV of EF-G and with ribosomal protein S12 (Fig. S11C). A $\sim 20^\circ$ rotation of domain II after EF-G binding was observed (Fig. 4C). More importantly, clear changes of the B2a inter-subunit

bridge were detected (Fig. 4D): through binding of C1913 (H69, helix 69 of 23S rRNA) with Gln23 (RRF), the loop of H69 was peeled away from h44 (helix 44 of 16S rRNA) by the 5 Å movement of A1912 (H69) from G1494 (h44) (Fig. S11D). These results indicate that EF-G binding induces the rotation of RRF domain II and the binding of H69 loop to RRF domain I, which jointly trigger the disruption of the inter-subunit bridge B2a.

4. Conclusions

In summary, here we studied the dynamics of RRF and its binding to PoTC on multiple time-scales by combined use of MD simulation, smFRET, and cryo-EM techniques. We found that RRF displayed two-layer dynamics: intra- and inter-molecular dynamics during ribosome splitting. The intra-molecular dynamics exhibited two different configurations of RRF: 'bent' and 'extended'. RRF alone was not highly dynamic, its domain II preferred to adopt the 'bent' conformation which was similar to that of the RRF in PoTC. This preference came from the interaction network of residue 61 at the linker region. Single-site mutation from aspartate to arginine could alter this interaction network and led to a more flexible RRF, namely the 'extended' form. The inter-molecular dynamics showed that the extended conformation of RRF was more beneficial for its binding to the PoTC but did not result in higher splitting activity due to its spatial clashes against EF-G. Only upon the interactions with the bent RRF, EF-G could push against RRF, thus to trigger the disruption of the major inter-subunit bridge B2a, and catalyze the splitting. Based on these results and previous work,

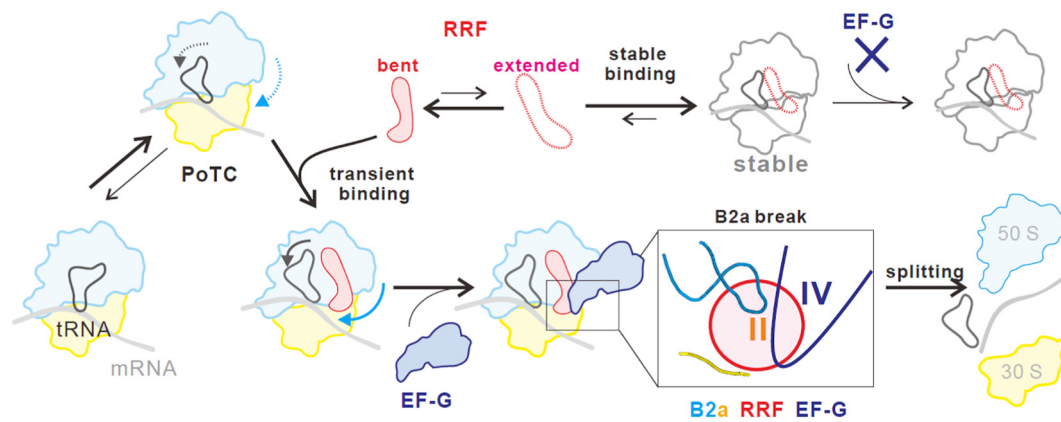


Fig. 5. Schematic model of ribosome recycling by two-layer dynamics of RRF and EF-G. Ribosomes in PoTC undergo spontaneous intersubunit rotational movement, equilibrated between ratcheted and unratcheted states. RRF alone is flexible, and can sample between bent and extended states which is regulated by the interaction network in its hinge region. Binding of bent RRF to the rotated PoTC is transient. Those RRFs with more flexible domain II bind to the PoTC with higher affinity, with its domain II orientation toward 50S. However, this orientation of RRF is not compatible for the subsequent EF-G binding, and thus blocks the splitting reaction. EF-G binding facilitates RRF reorientation and triggers the opening of the B2a bridge. The 70S ribosome is further split into two subunits completely after GTP hydrolysis.

we proposed an updated model for ribosome recycling (Fig. 5). PoTC ribosomes undergo spontaneous inter-subunit rotational movement, equilibrating between ratcheted and unratcheted states. RRF alone is relatively flexible and samples between bent (major) and extended (minor) states regulated by the interaction network in its hinge region. Binding of bent RRF to the PoTC is transient yet beneficial for the subsequent EF-G binding. Then EF-G pushes against RRF domain II to break the B2a bridge, and eventually disassembles the PoTC into the subunits. In contrast, extended RRF binds to the PoTC with higher affinity, with its domain II orientation toward 50S. However, this orientation of RRF is not compatible for the subsequent EF-G binding, and thus blocks the splitting reaction. In this model, the two layers of RRF dynamics play key roles in conformational activation of the PoTC and EF-G for subunits splitting and ribosome recycling.

Author statement

Guangtao Song: Data curation, Investigation, Methodology, Writing-Original draft preparation;

Benjin Xu: Data curation, Investigation, Methodology, Software;

Huigang Shi: Data curation, Investigation, Methodology, Software;

Yong Zhang: Data curation, Investigation, Methodology, Software;

Dejiu Zhang: Data curation, Investigation, Methodology, Software;

Xintao Cao: Data curation, Investigation, Methodology, Software;

Zengrui Liu: Data curation, Investigation;

Ran Guo: Data curation, Investigation;

Yan-Zhong Guan: Methodology, Supervision;

Yanhui Chu: Methodology, Supervision;

Xinzheng Zhang: Methodology, Supervision;

Jizhong Lou: Conceptualization, Methodology, Supervision, Writing-Reviewing and Editing;

Yan Qin: Conceptualization, Methodology, Supervision, Writing-Reviewing and Editing.

Acknowledgements

We thank Dr. L. He for technical assistance with the single-molecule FRET experiments. We thank B. Zhu, X. Huang, G. Ji, D. Fan, F. Sun, and the other staff at the Center for Biological Imaging (IBP, CAS) for their support in cryo-EM data collection. This work was supported by the National Key Research and Development Program of China (2018yfc1314400), Strategic Priority Research Programs (Category A) of the Chinese Academy of Sciences (XDA12010313), Key Research Program of Frontier

Sciences, CAS (QYZDB-SSW-SMC028), and National Natural Science Foundation of China (11672317, 31222022, 31500662, 81871041 and 81371463).

Declaration of competing interest

The authors declare no competing financial interest.

Appendix A. Supplementary data

Supplementary data to this article can be found online at <https://doi.org/10.1016/j.ijbiomac.2020.05.254>.

References

- [1] A. Korostelev, D.N. Ermolenko, H.F. Noller, Structural dynamics of the ribosome, *Curr. Opin. Chem. Biol.* 12 (2008) 674–683, <https://doi.org/10.1016/j.cbpa.2008.08.037>.
- [2] T.M. Schmeing, V. Ramakrishnan, What recent ribosome structures have revealed about the mechanism of translation, *Nature* 461 (2009) 1234–1242, <https://doi.org/10.1038/nature08403>.
- [3] A.S. Spirin, The ribosome as a conveying thermal ratchet machine, *J. Biol. Chem.* 284 (2009) 21103–21119, <https://doi.org/10.1074/jbc.X109.001552>.
- [4] A. Petrov, G. Kornberg, S. O'Leary, A. Tsai, S. Uemura, J.D. Puglisi, Dynamics of the translational machinery, *Curr. Opin. Struct. Biol.* 21 (2011) 137–145, <https://doi.org/10.1016/j.sbi.2010.11.007>.
- [5] R.M. Voorhees, V. Ramakrishnan, Structural basis of the translational elongation cycle, *Annu. Rev. Biochem.* 82 (2013) 203–236, <https://doi.org/10.1146/annurev-biochem-113009-092313>.
- [6] R.K. Agrawal, M.R. Sharma, M.C. Kiel, G. Hirokawa, T.M. Booth, C.M. Spahn, R.A. Grassucci, A. Kaji, J. Frank, Visualization of ribosome-recycling factor on the Escherichia coli 70S ribosome: functional implications, *Proc. Natl. Acad. Sci. U. S. A.* 101 (2004) 8900–8905, <https://doi.org/10.1073/pnas.0401904101>.
- [7] J.A. Dunkle, J.H. Cate, Ribosome structure and dynamics during translocation and termination, *Annu. Rev. Biophys.* 39 (2010) 227–244, <https://doi.org/10.1146/annurev-biophys.37.032807.125954>.
- [8] L. Janosi, I. Shimizu, A. Kaji, Ribosome recycling factor (ribosome releasing factor) is essential for bacterial growth, *Proc. Natl. Acad. Sci. U. S. A.* 91 (1994) 4249–4253, <https://doi.org/10.1073/pnas.91.10.4249>.
- [9] M. Selmer, S. Al-Karadaghi, G. Hirokawa, A. Kaji, A. Liljas, Crystal structure of Thermotoga maritima ribosome recycling factor: a tRNA mimic, *Science* 286 (1999) 2349–2352, <https://doi.org/10.1126/science.286.5448.2349>.
- [10] Y. Inokuchi, A. Hirashima, Y. Sekine, L. Janosi, A. Kaji, Role of ribosome recycling factor (RRF) in translational coupling, *EMBO J.* 19 (2000) 3788–3798, <https://doi.org/10.1093/emboj/19.14.3788>.
- [11] L. Lancaster, M.C. Kiel, A. Kaji, H.F. Noller, Orientation of ribosome recycling factor in the ribosome from directed hydroxyl radical probing, *Cell* 111 (2002) 129–140, <https://doi.org/10.1126/science.286.5448.2349>.
- [12] T. Yokoyama, T.R. Shaikh, N. Iwakura, H. Kaji, A. Kaji, R.K. Agrawal, Structural insights into initial and intermediate steps of the ribosome-recycling process, *EMBO J.* 31 (2012) 1836–1846, <https://doi.org/10.1038/emboj.2012.22>.
- [13] A. Borg, M. Pavlov, M. Ehrenberg, Complete kinetic mechanism for recycling of the bacterial ribosome, *RNA* 22 (2016) 10–21, <https://doi.org/10.1261/ma.053157.115>.

- [14] D. Zhang, K. Yan, Y. Zhang, G. Liu, X. Cao, G. Song, Q. Xie, N. Gao, Y. Qin, New insights into the enzymatic role of EF-G in ribosome recycling, *Nucleic Acids Res.* 43 (2015) 10525–10533, <https://doi.org/10.1093/nar/gkv995>.
- [15] Y. Zeng, Y. Cui, Y. Zhang, Y. Zhang, M. Liang, H. Chen, J. Lan, G. Song, J. Lou, The initiation, propagation and dynamics of CRISPR-SpyCas9 R-loop complex, *Nucleic Acids Res.* 46 (2018) 350–361, <https://doi.org/10.1093/nar/gkx1117>.
- [16] W. Humphrey, A. Dalke, K. Schulten, VMD: visual molecular dynamics, *J. Mol. Graph.* 14 (1996) 33–38, [https://doi.org/10.1016/0263-7855\(96\)00018-5](https://doi.org/10.1016/0263-7855(96)00018-5) (27–38).
- [17] A. Perez, I. Marchan, D. Svozil, J. Sponer, T.E. Cheatham 3rd, C.A. Loughton, M. Orozco, Refinement of the AMBER force field for nucleic acids: improving the description of alpha/gamma conformers, *Biophys. J.* 92 (2007) 3817–3829, <https://doi.org/10.1529/biophysj.106.097782>.
- [18] M. Zgarbova, F.J. Luque, J. Sponer, T.E. Cheatham 3rd, M. Otyepka, P. Jurecka, Toward improved description of DNA backbone: revisiting epsilon and zeta torsion force field parameters, *J. Chem. Theory Comput.* 9 (2013) 2339–2354, <https://doi.org/10.1021/ct400154j>.
- [19] X. Li, P. Mooney, S. Zheng, C.R. Booth, M.B. Braunfeld, S. Gubbens, D.A. Agard, Y. Cheng, Electron counting and beam-induced motion correction enable near-atomic-resolution single-particle cryo-EM, *Nat. Methods* 10 (2013) 584–590, <https://doi.org/10.1038/nmeth.2472>.
- [20] G. Tang, L. Peng, P.R. Baldwin, D.S. Mann, W. Jiang, I. Rees, S.J. Ludtke, EMAN2: an extensible image processing suite for electron microscopy, *J. Struct. Biol.* 157 (2007) 38–46, <https://doi.org/10.1016/j.jsb.2006.05.009>.
- [21] S.H. Scheres, A Bayesian view on cryo-EM structure determination, *J. Mol. Biol.* 415 (2012) 406–418, <https://doi.org/10.1016/j.jmb.2011.11.010>.
- [22] I.S. Gabashvili, R.K. Agrawal, C.M.T. Spahn, R.A. Grassucci, D.I. Svergun, J. Frank, P. Penczek, Solution structure of the E. coli 70S ribosome at 11.5 angstrom resolution, *Cell* 100 (2000) 537–549, [https://doi.org/10.1016/S0092-8674\(00\)80690-X](https://doi.org/10.1016/S0092-8674(00)80690-X).
- [23] E.F. Pettersen, T.D. Goddard, C.C. Huang, G.S. Couch, D.M. Greenblatt, E.C. Meng, T.E. Ferrin, UCSF Chimera—a visualization system for exploratory research and analysis, *J. Comput. Chem.* 25 (2004) 1605–1612, <https://doi.org/10.1002/jcc.20084>.
- [24] S.M. Stagg, S.C. Harvey, Exploring the flexibility of ribosome recycling factor using molecular dynamics, *Biophys. J.* 89 (2005) 2659–2666, <https://doi.org/10.1529/biophysj.104.052373>.
- [25] M. Selvaraj, A. Govindan, A. Seshadri, B. Dubey, U. Varshney, M. Vijayan, Molecular flexibility of Mycobacterium tuberculosis ribosome recycling factor and its functional consequences: an exploration involving mutants, *J. Biosci.* 38 (2013) 845–855, <https://doi.org/10.1007/s12038-013-9381-0>.
- [26] S.H. Sternberg, J. Fei, N. Prywes, K.A. McGrath, R.L. Gonzalez Jr., Translation factors direct intrinsic ribosome dynamics during translation termination and ribosome recycling, *Nat. Struct. Mol. Biol.* 16 (2009) 861–868, <https://doi.org/10.1038/nsmb.1622>.
- [27] J.A. Dunkle, L. Wang, M.B. Feldman, A. Pulk, V.B. Chen, G.J. Kapral, J. Noeske, J.S. Richardson, S.C. Blanchard, J.H. Cate, Structures of the bacterial ribosome in classical and hybrid states of tRNA binding, *Science* 332 (2011) 981–984, <https://doi.org/10.1126/science.1202692>.
- [28] K. Atarashi, A. Kaji, Inhibitory effect of heterologous ribosome recycling factor on growth of Escherichia coli, *J. Bacteriol.* 182 (2000) 6154–6160, <https://doi.org/10.1128/jb.182.21.6154-6160.2000>.
- [29] V.S. Raj, H. Kaji, A. Kaji, Interaction of RRF and EF-G from E-coli and T-thermophilus with ribosomes from both origins - insight into the mechanism of the ribosome recycling step, *RNA* 11 (2005) 275–284, <https://doi.org/10.1261/rna.7201805>.
- [30] Z. Fu, S. Kaledhonkar, A. Borg, M. Sun, B. Chen, R.A. Grassucci, M. Ehrenberg, J. Frank, Key intermediates in ribosome recycling visualized by time-resolved cryoelectron microscopy, *Structure* 24 (2016) 2092–2101, <https://doi.org/10.1016/j.str.2016.09.014>.